Journal of Molecular Structure 1312 (2024) 138633

Contents lists available at ScienceDirect

Journal of Molecular Structure

journal homepage: www.elsevier.com/locate/molstr

Synthesis and photoluminescence study of two new complexes Er^{3+} and Yb^{3+} and their PMMA based composite fibers

Ugur Erkarslan [a,*], Gorkem Oylumluoglu [a], Ozay Eroglu [b], Mustafa Burak Coban [c], Hulya Kara Subasat [b]

[a] Department of Physics, Faculty of Science, Molecular Nano-Materials Laboratory, Mugla Sıtkı Koçman University, Mugla, Turkiye
[b] Department of Energy, Graduate School of Natural and Applied Sciences, Mugla Sıtkı Kocman University, Mugla, Turkiye
[c] Department of Physics, Faculty of Science and Art, Balikesir University, Balikesir, Turkiye

ARTICLE INFO

Keywords:
Electrospinning
Er^{3+} and Yb^{3+}
Luminescent fiber
Poly(methyl methacrylate (PMMA)
Crystal structure

ABSTRACT

The present article showcases the creation and evaluation of luminescent composite fibers by embedding coordination polymers, such as Er(**1**) $\{[Er(2\text{-stp})_3(H_2O)]\}_n$ and Yb(**2**) $\{[Yb(2\text{-stp})_3(H_2O)]\}_n$, which are suspended in 2-sulfoterephthalate, into polymer matrices using electrospinning. The Er(**1**) and Yb(**2**) complexes were combined with poly (methyl methacrylate) (PMMA) at concentrations ranging from 5 wt.% to 25 wt.%, leading to the formation of Er@PMMA and Yb@PMMA fibers. This method resulted in one-dimensional (1D) luminescent composite fibers. Our study reveals that these composite fibers exhibit superior photoluminescence properties compared to their individual pure complex counterparts. This enhancement is ascribed to the synergistic effects of the PMMA matrix and electrospun fiber structure. Furthermore, we observed that the composite nanofibers exhibited significantly better thermal and photostability compared to their pure complexes.

1. Introduction

Lanthanide luminescent rare earth complexes are esteemed for their unique properties, such as sharply defined emission peaks, significant Stokes shifts, and extended excited state durations. Their emission, primarily from f-f transitions, features extremely narrow bandwidths that lead to the emission of highly pure colors [1]. These characteristics in lanthanide complexes have surged due to their potential in a variety of applications, including as luminescent probes, in drug delivery, optoelectronics, optical communications, and sensors [2]. Er^{3+} ions are notable for their efficient yellow luminescence, applicable in areas like solid-state lighting, field emission displays, security printing, and both biological and sensing applications [3]. Similarly, Yb^{3+}ions, with their near-infrared (NIR) luminescence around 980 nm, are regarded as highly promising for applications in bioanalytical research, telecommunications, and laser designs [4].

However, the challenge with Ln^{3+}doped inorganic materials is their low absorption density, which has prompted the exploration of methods to enhance their light absorption capabilities. Integrating suitable organic ligands into Ln^{3+} complexes is an effective strategy to facilitate energy transfer upon excitation, thereby increasing the luminescence of these materials. Aromatic carboxylic acid ligands, which feature multiple coordination atoms like N and O, offer several coordination sites and modes, improving the water solubility of the complexes due to their carboxylic acid groups [5]. Additionally, these ligands allow for the introduction of active groups into the aromatic ring, expanding the complexes' application possibilities. Direct use of β-diketone complexes in materials is limited by their processing challenges, thermal instability, and mechanical weakness. However, the addition of these complexes to organic, inorganic, or hybrid composite materials has broadened their applicability. Incorporating these complexes into polymers or using electrospinning technology to create nanofibers significantly enhances the materials' thermal stability, mechanical strength, and luminescence properties [6–8].

A comprehensive survey of methodologies for fabricating luminescent nanocomposites reveals the application of diverse techniques, including but not limited to self-assembly, solution casting, phase separation, melt blowing, and chemical synthesis [9–11]. Within this spectrum of methodologies, electrospinning emerges as a preeminent technique, distinguished by its simplicity and efficacy in generating

* Corresponding author at: Department of Physics, Faculty of Science, Molecular Nano-Materials Laboratory, Mugla Sıtkı Koçman University, 48170, Mugla, Turkey.
E-mail address: eugur@mu.edu.tr (U. Erkarslan).

https://doi.org/10.1016/j.molstruc.2024.138633
Received 12 March 2024; Received in revised form 21 April 2024; Accepted 13 May 2024
Available online 14 May 2024

continuous one-dimensional hybrid composite fibers at the nanometer scale [9]. The adaptability of electrospinning permits the attainment of a broad array of structural configurations, such as porous fibers, ribbon-like formations, wrinkled structures, and beaded fibers, through the precise modulation of the electrospinning parameters [12]. Significantly, electrospinning has been effectively employed in the synthesis of luminescent composite fibers exhibiting tailored optical properties. This has been achieved through the use of various polymers, including Polyvinyl Alcohol (PVA), Polyethylene Oxide (PEO), Polyvinylpyrrolidone (PVP), and, Polymethyl Methacrylate (PMMA) underscoring the method's versatility and its pivotal role in advancing the field of composite material science. Polymethyl Methacrylate (PMMA) stands as a versatile polymer with promising applications across a diverse array of fields, including but not limited to, optical technologies, pneumatic actuation systems, sensor development, analytical separation methodologies, and conductive device fabrication [13].

This research focuses on the fabrication of photoactive composite fibers containing coordination polymers with Er(**1**) and Yb(**2**) complexes, embedded within a PMMA matrix through electrospinning. The photoluminescence properties of these fibers were thoroughly examined, demonstrating enhanced performance over their pure complex counterparts. Moreover, we anticipate that the outcomes of this study will not only yield fresh insights into luminescent behavior but also unlock possibilities for innovative applications in the realm of optoelectronic devices and beyond.

2. Experimental details

2.1. Materials and physical measurements

$Er(NO_3)_3{\cdot}5H_2O$ with a purity of 99.9%, Poly(methylmethacrylate) PMMA with a molecular weight of approximately 350.000, NaOH with a purity of 98%, N,N-Dimethylformamide (DMF) with a purity of 99.8%, and ethanol with a purity of 99.8% were purchased from Sigma-Aldrich. $YbCl_3{\cdot}6H_2O$ with a purity of 99.9% was obtained from Fluorochem Ltd., and 2-sulfoterephthalic acid monosodium salt (2-NaH_2stp) was procured from TCI.

Elemental analysis was conducted using an Elementar Vario-EL-III microanalyzer, and Fourier Transform Infrared (FT-IR) spectral data were obtained using a Perkin Elmer Spectrum 65 spectrophotometer in conjunction with an ATR-Kit system. The spectral data were collected over a range of 4000–600 cm^{-1} at room temperature. The thermal stability of the sample was evaluated using a PerkinElmer TGA 4000 thermogravimetric analyzer. The FEI QUANTA 250 FEG, which was outfitted with an energy-dispersive spectroscopy (EDX) system, was utilized to capture the SEM images. The Image J software was employed to ascertain the average diameter and size distribution of the composite fibers depicted in the SEM images. The ANDOR SR500i-BL luminescence spectrometer, equipped with a triple grating and an Intensified Charge Coupled Device (ICCD) camera for the visible region, and an InGaAs detector for the near-infrared (NIR) region, was utilized to measure the photoluminescence (PL) spectra.

The frequency-tripled Nd:YLF Q-switched pulse laser operating at 349 nm was utilized as the laser source for excitation. The powder X-ray diffraction (PXRD) patterns were captured using a Philips PW-1710/00 diffractometer and Cu-Kα radiation (λ = 1.5418 Å) in the range of $5^\circ < 2\theta < 50^\circ$ The data was collected in the θ-θ mode with a step size of 5 $s < n < 10$ s and a step width of 0.03° The experimental PXRD patterns were compared to the calculated patterns obtained from CIF files using Mercury 3.9. [14].

The X-ray diffraction data for both the Er(**1**) and Yb(**2**) complexes were acquired using a Xcalibur, Eos diffractometer with MoKα monochromatic radiation (λ=0.71073 Å) at room temperature. The structure was determined using both the direct method and the full-matrix least-squares method on F^2 with the aid of Olex2–1.2 software [15]. Olex2–1.2 was also utilized to refine the positions of all non-hydrogen atoms through anisotropic atomic displacements. When refining the hydrogen atoms, they were either incorporated using their idealized geometry or placed in the difference Fourier map and refined "riding" on the corresponding parent atoms. The Olex2–1.2 software's MASK procedure was employed to account for the influences of disordered solvent molecules, and the free model of this procedure was implemented for the concluding refinement process. The chemical formula for Er(**1**) comprised three water molecules, whereas the formula for Yb(**2**) comprised one water molecule and one methanol molecule, along with their respective hydrogen atoms, which were excluded from the total chemical formula and the list of atoms.

Geometric calculations were conducted using the software PLATON 1.17 [16], while molecular visuals were generated with the aid of Olex2–1.2. The crystal data and structure refinement information for both complexes are presented in Table 1. Bond lengths and angles for selected components are listed in Table 2. The coordination modes of the 2-stp ligand for Er(**1**) and Yb(**2**) are detailed in Scheme S1. The molecular structure of Er(**1**) and Yb(**2**) with atomic labeling is illustrated in Fig. 1 and Fig. S1, respectively, while the packing diagrams are provided in Fig. 2 and Fig. S2, respectively. A schematic representation of the synthesis process for Er@PMMA and Yb@PMMA nanofibers is shown in Scheme 1.

2.2. Synthesis of Er(*1*) and Yb(*2*)

The preparation of two complexes, $Er(NO_3)_3{\cdot}5H_2O$ and $YbCl_3{\cdot}6H_2O$, was carried out using established methods as documented in the literature [3,17,18]. A solution of 2-stp (0.1 mmol) and $Er(NO_3)_3{\cdot}5H_2O$ (0.1 mmol) was prepared by dissolving both reagents in 10 ml of distilled water and methanol, with constant stirring. Subsequently, a 1 mol/L NaOH solution was added to the mixture, and stirring was continued. The mixture was then heated at 30 °C for 5 h before being transferred to a bomb equipped with a Teflon liner (45 ml) and heated at 120 °C for 3 days. After cooling to room temperature, the product was filtered and washed with distilled water to yield crystals of Er(**1**) (pink) and Yb(**2**) (yellow).

2.3. Preparation of composite fibers

Poly(methyl methacrylate) (PMMA) was dissolved in N,N-dimethylformamide (DMF) to prepare a 15 wt.% solution. Subsequently, Er(**1**) and Yb(**2**) complexes were added to the above mixture solution in amounts corresponding to 5, 10, 15, and 20 wt.% by weight PMMA. The resulting solution was stirred for 12 h at room temperature to ensure homogeneity and transparency.

Electrospinning was conducted using a laboratory spinning unit

Table 1
Crystal data and structure refinement information for Er(**1**) and Yb(**2**).

	1	**2**
Chemical Formula	$C_8H_9ErO_{10}S$	$C_8H_9O_{10}SYb$
Formula weight (g mol^{-1})	464.47	470.25
Crystal system, space group	Orthorhombic, *Pbcn*	Orthorhombic, *Pbcn*
Unit cell dimensions	a = 19.8224 (8) Å b = 7.3738 (3) Å c = 19.4844 (7) Å	a = 19.7704 (8) Å b = 7.3549 (3) Å c = 19.3952 (8) Å
V / $Å^3$	2847.97 (2)	2820.2 (2)
Z	8	8
ρ_{calc} / g cm^{-3}	2.167	2.215
μ/mm^{-1}	6.08	6.82
Temperature (K)	292	294
Reflections collected	5760	6497
Independent reflections	2682, [R_{int}=0.026]	2666, [R_{int}=0.036]
Goodness–of–fit on F^2	1.03	1.026
R indices [$I > 2\sigma(I)$]	R_1 = 0.0272, wR_2 = 0.0600	R_1 = 0.0312, wR_2 = 0.0642

Table 2
Selected bond lengths (Å) and bond angles (°) of Er(**1**) and Yb(**2**).

1		2	
Er-O_w	2.333(3)- 2.425(3)	Yb-O_w	2.298(4)- 2.408(4)
Er-O_{CO2}	2.256 (3)- 2.444 (3)	Yb-O_{CO2}	2.239(3)- 2.424(4)
Er-O_{SO3}	2.305 (3)	Yb-O_{SO3}	2.283(3)
O_w-Er-O_w	71.92 (12) - 144.11(12)	O_w-Yb-O_w	73.53(14)- 143.98 (14)
O_w-Er-O_{CO2}	69.33(12)- 146.41(12)	O_w-Yb-O_{CO2}	69.53(14)- 146.31 (14)
O_w-Er-O_{SO3}	70.75(11) - 95.39(12)	O_w-Yb-O_{SO3}	71.21(13)- 95.02(14)
O_{CO2}-Er-O_{CO2}	53.76(12)- 132.75(12)	O_{CO2}-Yb-O_{CO2}	54.24(14)- 132.51 (15)
O_{CO2}-Er-O_{SO3}	78.35(11) - 160.63(11)	O_{CO2}-Yb-O_{SO3}	78.78(13)- 160.45 (13)

(SPINGENIX SG-1) and a 15.5 kV DC high-voltage generator in a horizontal alignment. The spinning solution was then ejected through a 5 mL plastic injector with a non-rust steel needle having an inner diameter of 0.8 mm. The distance between the collector and the needle tip was set at 20 cm, and the fluid supply rate was set at 2 mL/h. The randomly arranged nanofibers were collected on an electrically grounded aluminum foil. Finally, the composite fibers were dried in a vacuum-drying oven at 40 °C for 12 h to remove any residual organic solvent.

3. Results and discussion

3.1. Crystal structure

The crystal structure data obtained from X-ray diffraction analysis demonstrate that the compounds Er(**1**), which is composed of $[Er(2\text{-stp})\cdot 3(H_2O)]_n$, and Yb(**2**), which is composed of $[Yb(2\text{-stp})\cdot 3(H_2O)]_n$, have the same crystal structure and belong to the orthorhombic system with the *Pbcn* space group. For the purpose of this analysis, we will focus on Er(**1**). The asymmetric unit of Er(**1**) comprises an Er^{3+} ion, a 2-stp ligand, and three water molecules that are coordinated to the Er^{3+} ion. The Er^{3+} ion exhibits octahedral coordination and assumes a distorted square-antiprismatic geometry. It incorporates four oxygen atoms from the carboxylate groups with Er-O_{CO2} bond lengths ranging from 2.256 (3) to 2.444 (3) Å, a single oxygen atom from the sulfonato group with an Er-O_{SO3} bond length of 2.305 (3) Å, and three oxygen atoms from coordinated water molecules with Er-O(w) bond lengths varying from 2.333(3) to 2.425(3) Å (Fig. 1). The bond lengths and angles in this study are consistent with previously reported values for similar complexes [3,19] (Table 2), as demonstrated by the results obtained.

The 2-stp ligand in both Er(**1**) and Yb(**2**) consistently adopts the coordination mode shown in Scheme S1. Upon deprotonation, the carboxylate and sulfonato groups coordinate with three distinct Er^{3+} ions for Er(**1**) or Yb^{3+} ions for Yb(**2**). Specifically, for Er(**1**), the O9-C8-O10 group forms a bis(bidentate) coordination mode, where the O9 and O10 atoms are bonded to a single Er^{3+} ion, while the O4-C1-O5 group participates in a monodentate coordination mode, with the O4 atom binding to one Er^{3+} ion and the O5 atom to another. This leads to the formation of a two-dimensional network for Er(**1**) within the *bc* plane, as depicted in Fig. 2.

Previously, researchers documented crystal structures similar to those under discussion, specifically $[Ln(TPSO_3)\cdot(H_2O)_2]_n$, where $TPSO_3$ is sulfonatoterephthalate [19]. To examine the photoluminescence characteristics of the Er(**1**) and Yb(**2**) complexes, as well as their composite fibers with Poly(methyl methacrylate) (PMMA), denoted as Er@PMMA and Yb@PMMA, respectively, we synthesized these complexes and elucidated their crystal structures. Notably, the single crystal data for the structures reported earlier were collected at 100 K and were associated with a triclinic space group (P-1), whereas the crystallographic analysis conducted in the present study was carried out at room temperature and pertained to an orthorhombic space group (*Pbcn*). Consequently, there is a divergence in the single crystal structural data between this study and those reported previously.

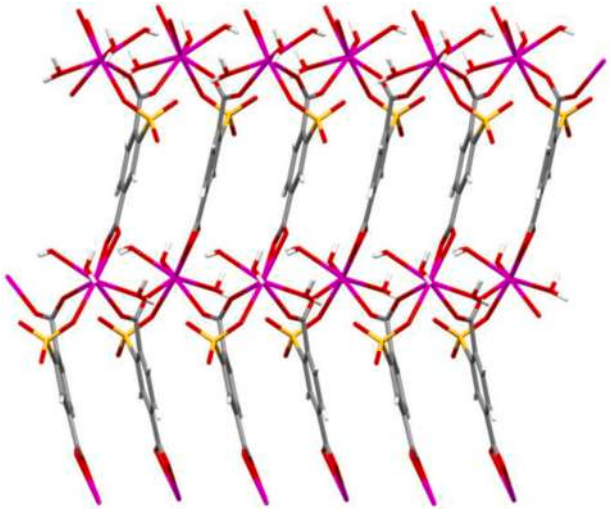

Fig. 2. A view of 2-D network of Er(**1**) in *bc* plane.

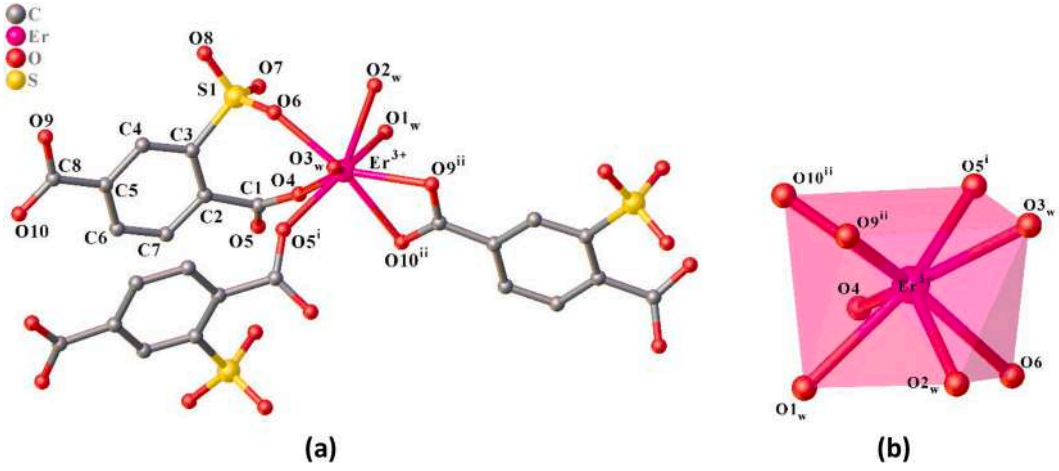

Fig. 1. (a) The molecular structure of Er(**1**). H atoms have been omitted for clarity, **(b)** Distorted square-antiprismatic geometry surrounding the Er^{3+} atom in Er(**1**).

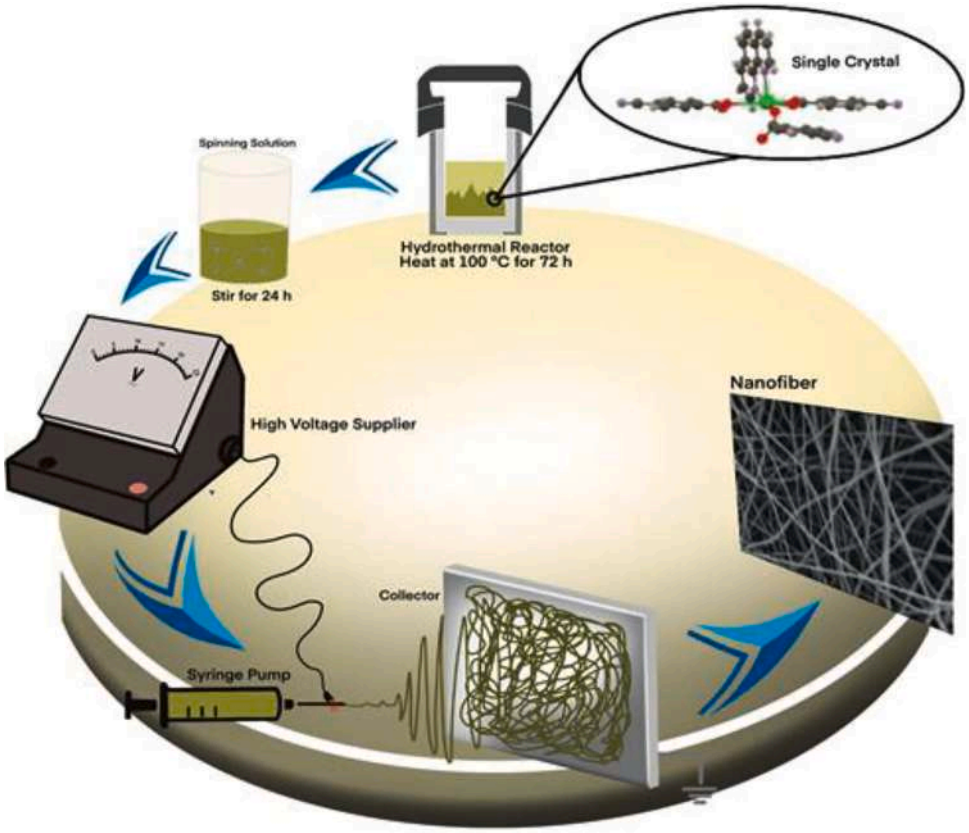

Scheme 1. Schematic presentation of the preparation of Er@PMMA and Yb@PMMA nanofibers.

3.2. Powder X-ray diffraction and FTIR analysis

Powder X-ray diffraction (PXRD) measurements provide valuable information regarding the purity of synthesized complexes. By comparing the XRD patterns of Er(**1**) and Yb(**2**) to simulated patterns (Fig. S3), it is evident that the phase purity of both complexes is high.

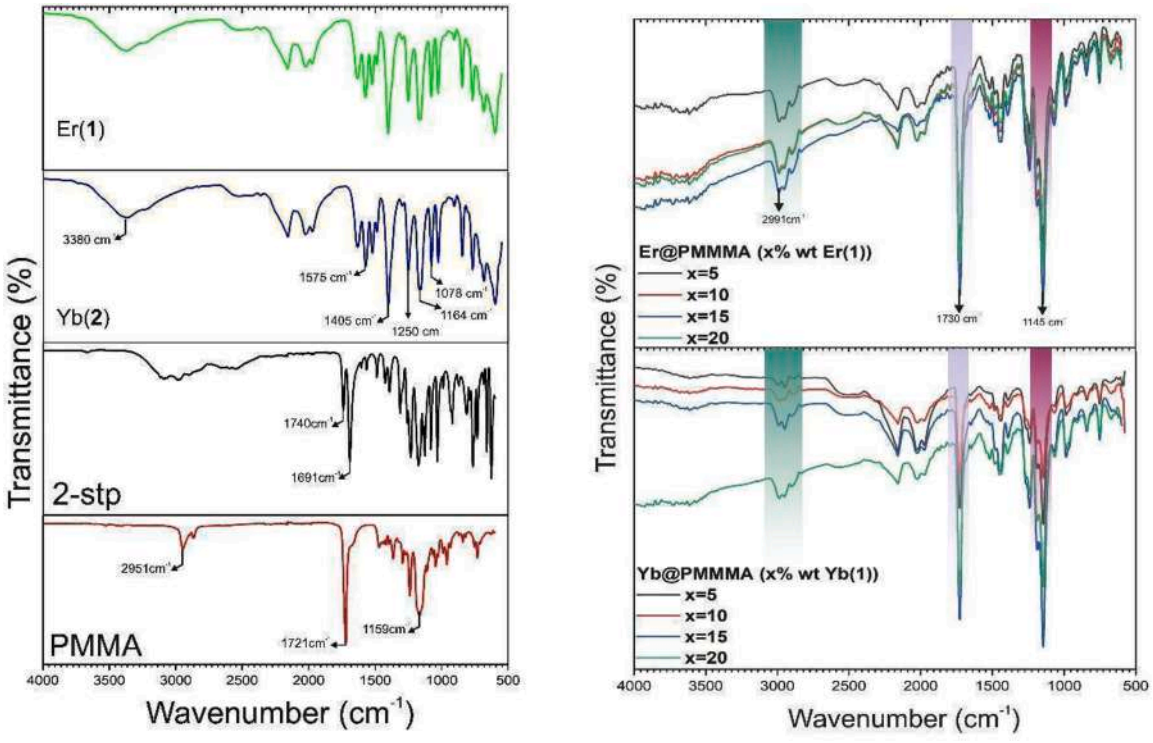

Fig. 3. FT-IR spectra of 2-stp and PMMA (a) Er(**1**) and Yb(**2**) (b) Er@PMMA and Yb@PMMA.

Based on this observation, it can be concluded that the PXRD measurements of the synthesized complexes are effective in determining their purity.

The bond properties and chemical bond formations between the dopant and the host polymer in Er@PMMA and Yb@PMMA fibers (5 wt. % – 25 wt.%), as well as their pure complexes and precursors, were analyzed using FTIR (Fig. 3). As the complexes and nanofibers exhibited almost identical behavior across all spectra, only Er(**1**), its fibers and free ligands will be discussed in detail as representative examples. For the Er (**1**) complex, the asymmetric and symmetric stretching vibrations of the carboxylate ions were identified at 1575 and 1405 cm^{-1}, with the difference in these vibrations being approximately 160 cm^{-1}. This value is significantly lower than the typically expected 200 cm^{-1}, suggesting that the carboxyl groups are chelated to the Er(**1**) ions [3]. The inference of coordinated water molecules in the Er(**1**) complex was based on the mid-peak around 3380 cm^{-1} in its spectrum, suggesting the presence of ν(O—H) stretching frequencies [20]. Furthermore, the absorption bands at 1250, 1164, and 1078 cm^{-1} indicate typical stretching vibrations of SO_3 groups, aligning with the crystalline structure of the Er(**1**) complex.

The pristine polymethyl methacrylate (PMMA) matrix is distinguished by four prominent absorption bands within its infrared spectrum. This spectral profile is marked by two pronounced bands, attributed to the stretching vibrations of the carbonyl group (C = O) at 1721 cm^{-1} and the ester group (C—O) at 1159 cm^{-1}, respectively [7,21]. The spectral range from 2951 cm^{-1} covers vibrational bands related to the stretching modes of the C—H bonds. The peak attributed to the C = O stretching band in PMMA at 1721 cm^{-1} shows a notable shift to a lower frequency at 1730 cm^{-1} in the Er@PMMA composite fibers. This shift suggests an interaction between the oxygen atoms of the carbonyl group in PMMA and the Er^{3+} ions in the Er(**1**) complex [22,23]. Additionally, the diminished absorption peak at 1145 cm^{-1} in the Er@PMMA fibers, attributed to the overtone of the C = O stretching mode in 2-stp, indicates the successful doping of the Er(**1**) complex into PMMA [6].

3.3. Morphology of analysis of composite fibers

The SEM was utilized to examine the surface morphologies of electrospun products Er@PMMA and Yb@PMMA, which contain varying

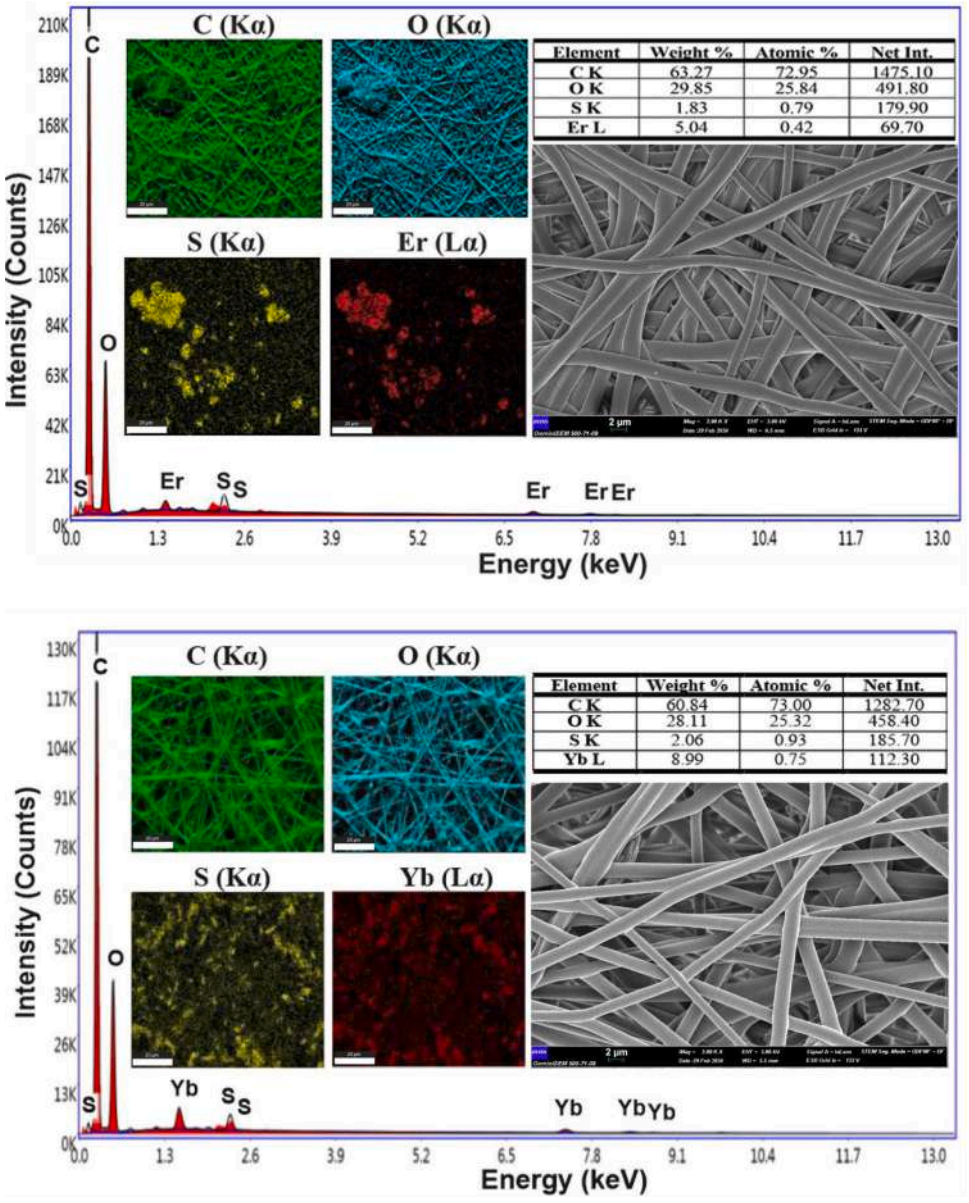

Fig.4. A) SEM images and EDX of optimized of Er@PMMA (10 wt.%) and elemental mapping of carbon (C), oxygen (O), sulphur (S), erbium (Er) and B) SEM images and EDX of optimized of Yb@PMMA (15 wt.%), carbon (C), oxygen (O), sulphur (S), ytterbium (Yb).

concentrations of the Er(**1**) and Yb(**2**) complexes. Fig. 4 displays SEM images and EDX spectroscopy of the optimized Er@PMMA and Yb@PMMA samples. Additionally, Figure S4 presents SEM images and a size distribution graph for both Er@PMMA and Yb@PMMA, respectively. The observed average diameters of the one-dimensional (1D) composite fibers exhibited an increase from 1.29 μm (at 5 wt.%) to 1.99 μm (at 25 wt.%) for Er@PMMA, and from 1.74 μm (at 5 wt.%) to 2.14 μm (at 25 wt.%) for Yb@PMMA. The SEM histograms indicate that

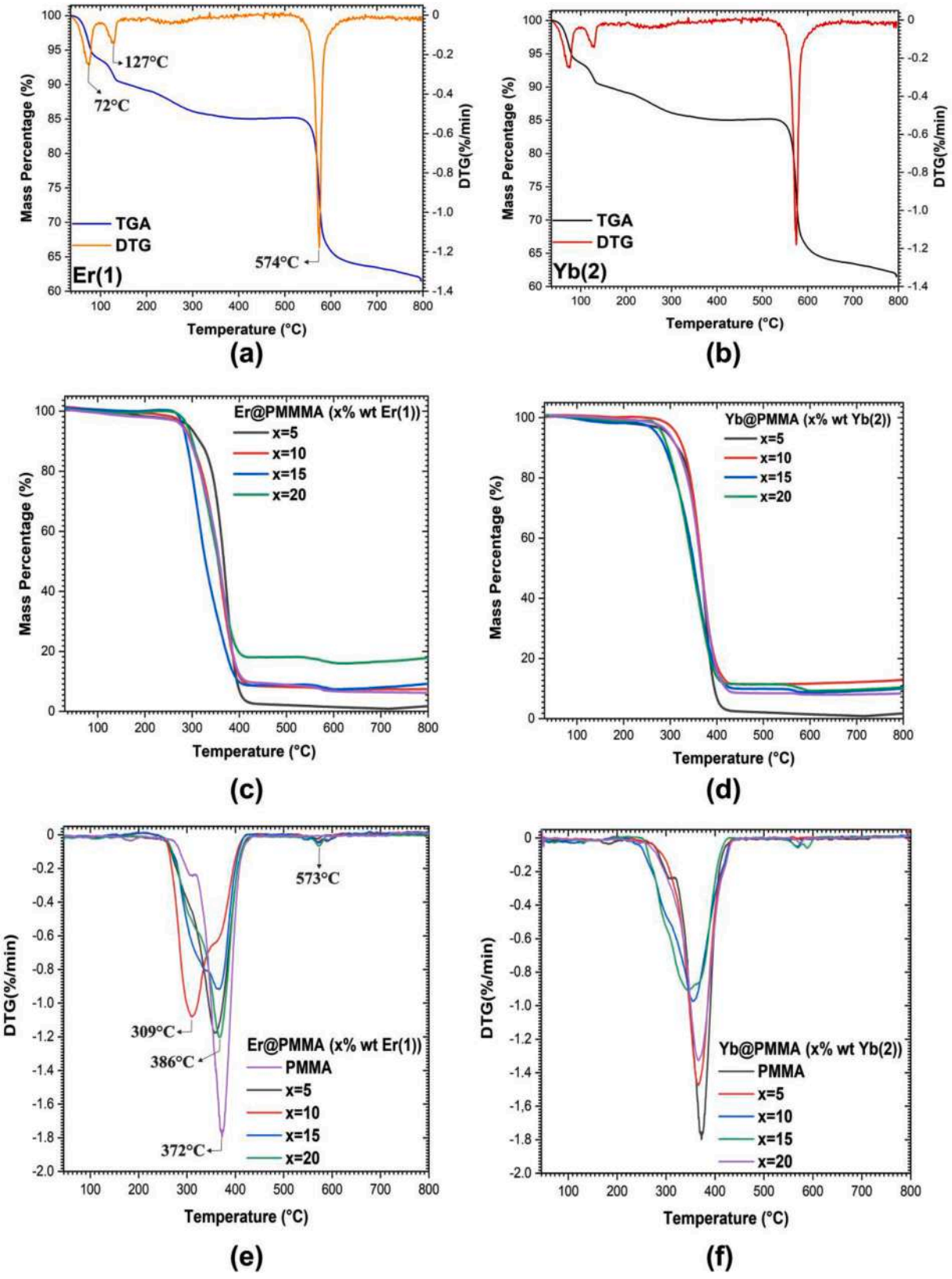

Fig. 5. TGA-DTG curve of (a) Er(**1**), (b) Yb(**2**), (c,e) Er@PMMA, (d,f) Yb@PMMA.

the integration of Er(**1**) and Yb(**2**) complexes into the PMMA matrix led to an increase in the solution viscosity and enhanced the electrical conductivity of the soluble materials. This enhancement in viscosity and conductivity resulted in the aggregation of fibers during the electrospinning process, which subsequently led to an increase in the diameters of the fibers [24,25]. SEM images depict that the surfaces of the Er@PMMA and Yb@PMMA composite fibers are predominantly smooth, albeit with a minority of fibers appearing relatively irregular and rough. Hence, the increase in the diameter of the composite fibers, as evidenced in the SEM images, confirms the successful amalgamation of the Er(**1**), Yb(**2**) complexes, and the PMMA polymer matrix. This outcome indicates that the Er(**1**) and Yb(**2**) complexes were uniformly dispersed within the PMMA matrix, suggesting a high level of compatibility with the PMMA polymer, which holds potential implications for the material's properties and applications.

Energy Dispersive X-ray Spectroscopy (EDX) serves as a pivotal technique for determining the elemental composition within specific regions of a sample and has been extensively employed in this study to authenticate the homogeneous synthesis of Er@PMMA and Yb@PMMA composite fibers. The procedure involved scrutinizing designated regions of interest during the EDX analysis, which unveiled peaks indicative of the elements inherent to the precursor materials. The EDX findings corroborated the presence of carbon (C), oxygen (O), sulfur (S), and the respective lanthanide elements erbium (Er) for Er(**1**) or ytterbium (Yb) for Yb(**2**) within the electrospun products.

The unequivocal integration of the Er(**1**) and Yb(**2**) complexes into the PMMA matrix was evidenced through distinct spectral peaks in the EDX spectrum, as depicted in Fig. 4. These peaks distinctly matched the elements within the examined region of interest. Furthermore, the atomic and weight percentages of the elements in the composite fibers were quantified, with the results succinctly presented in a tabulated inset within the EDX plot (Fig. 4). The observation of consistent peaks across the spectrum is indicative of the formation of stable fibers that possess the correct atomic distribution, a crucial aspect for the advancement of subsequent optical and structural investigations [26]. Moreover, these findings lend substantial support to the analyses concerning luminescence and structural properties [27].

3.4. TGA and DTG analysis

Thermogravimetric Analysis (TGA) and differential thermogravimetry (DTG) have been used as a critical technique for analyzing the thermal stability and decomposition characteristics of organic-inorganic hybrid materials [28]. This analysis was conducted to evaluate the thermal behavior of pure Er(**1**) and Yb(**2**) complexes, as well as PMMA and related composite fibers, across a range from room temperature to 800 °C under a nitrogen atmosphere, and the findings are presented in Fig. 5. The thermal properties of pure Er(**1**), Yb(**2**) complexes, and their PMMA composite fibers have shown consistent and uniform characteristics. The pure Er(**1**) and Yb(**2**) complexes displayed analogous thermal decomposition profiles, characterized by multiple stages of mass loss (Fig. 5a and 5b). The DTG curve of Er(**1**) and Yb(**2**) shows two maximum T_{max} signals (at 72 and 127 °C), followed by one signal at 574 °C, which corresponds to maximum decomposition rates. The sum of both mass reductions of 8.5% occurring from room temperature to 140 °C is attributable to the evaporation of lattice water molecules. This is succeeded by a subsequent mass loss of approximately 15% at 350 °C. Between 350 and 537 °C, the structures exhibit relative thermal stability. The last signal leads to another mass loss of ~35%, which occurs at 574 °C. This can be interpreted as a decomposition of the ligand and the coordination polymer framework beginning to collapse. A pronounced mass loss, 62.7% for Er(**1**) and 62.8% for Yb(**2**) was recorded at 750 °C. As a result, we speculate that the final residual weight likely originated from Er^{3+}/Yb^{3+} oxide.

Furthermore, the thermal degradation pattern of the PMMA polymer fiber without any additives occurred in one step with a maximum rate peak in DTG curves, whereas the thermal decomposition of Er/Yb@PMMA nanofibers followed a two-step degradation reaction degradation reaction, as shown in Fig. 5c-f. For the PMMA polymer fiber, decomposition occurred between 245 and 420 °C (the maximum degradation temperature T_{max}=372 °C). The Er/Yb@PMMA was presented with two main steps of degradation. The first step was between T_{max} = 309 and 386 °C, with mass loss of about 85–90 wt.% attributed to the cleavage of the polymer's large molecular chains into smaller units and the separation of weak head-to-head bonds at the ends of the chains. The second step was placed between 558 and 612 °C (T_{max}=573 °C). This DTG peak is the degradation process occurring in Er/Yb compounds. As a result, the incorporation of Er(**1**) and Yb(**2**) complexes into the PMMA matrix leads to a notable shift in the degradation temperatures towards higher values. This alteration is attributed to the rearrangement of polymer chains around the dopant complexes, which enhances the composite's capacity for heat dissipation [29].

3.5. Photoluminescence properties

PL spectroscopy is an effective method that provides invaluable insights into the role of electron pair recombination and supplies essential information about the optical properties of a substance. In this study, we investigated the luminescent properties of the free ligand (2-stp), PMMA, Er(**1**), and Yb(**2**) complexes, as well as their composite fibers (Er@PMMA and Yb@PMMA) under 349 nm laser illumination in the visible and/or near-infrared (NIR) regions at room temperature. As a proof-of-concept, we measured the concentration-dependent emission spectra of Er(**1**) and Yb(**2**) doped PMMA polymer matrixes as the concentration increased from 5 wt.% to 20 wt.% by monitoring a broad spectral region. The results are presented in Fig. 6. The luminescence emission spectra of free ligand 2-stp and polymer of PMMA are characterized by a broad Ligand-centered charge transfer (ILCT) band with maximum intensity at 500–530 nm, which has the same excitation mechanism as other free ligands and polymer matrixes (Fig. S5). The emissions in question are linked to the electronic transition of the n-π^* or π-π^* [17,30,31].

To ensure that the luminescence emissions from both samples were comparable within their respective groups, we maintained the position and intensity of the excitation light source constant when characterizing them. The Er(**1**) samples exhibited bright pink luminescence that was easily visible to the naked eye. As shown in Fig. 6a and 6b, all the Er(**1**) samples displayed important characteristic emission peaks in the Vis-NIR region. The green and red emission peaks at 547 nm and 680 nm, respectively, correspond to the $^4S_{3/2} \rightarrow {}^4I_{15/2}$ and $^4F_{9/2} \rightarrow {}^4I_{15/2}$ transitions of Er^{3+}, respectively [32]. Notably, the red peak was significantly higher than the green peak [32]. Additionally, the material emitted strong 1528 nm luminescence, originating from the $^4I_{13/2} \rightarrow {}^4I_{15/2}$ transition of Er^{3+} ions [33,34].

The near-infrared (NIR) region is where the PL spectra of Yb(**2**) are observed (Fig. 6c), specifically at 980 nm, which corresponds to the $^2F_{5/2} \rightarrow {}^2F_{7/2}$ transitions of Yb^{3+}–Yb^{3+} pairs (as shown in Fig. 6d). The energy level structure of the Yb^{3+} ion's f-f system is straightforward, comprising only two states: the $^2F_{7/2}$ ground multiplet and the $^2F_{5/2}$ excited state, which lies at approximately 10.000 cm^{-1}. The absence of absorption in the visible range, as well as the lack of up-conversion and excited state absorption, is observed when the effective laser cross-section is reduced. The Yb complexes are appealing for use in laser operation and ionic crystals and glasses due to their intense absorption and emission properties [35–37].

To determine the optimal doping concentration for the greatest luminescence in Ln@PMMA, we can compare the emission intensity of Er^{3+} and Yb^{3+} doped samples at varying concentrations. According to Fig. 6, the optimal concentration for Er^{3+} ions is 0.15, while for Yb^{3+} ions it is 0.10. The results show that the luminescence intensity of Er^{3+}increases initially and reaches its peak at 15% doping concentration, whereas the luminescence intensity of Yb^{3+} reaches its maximum

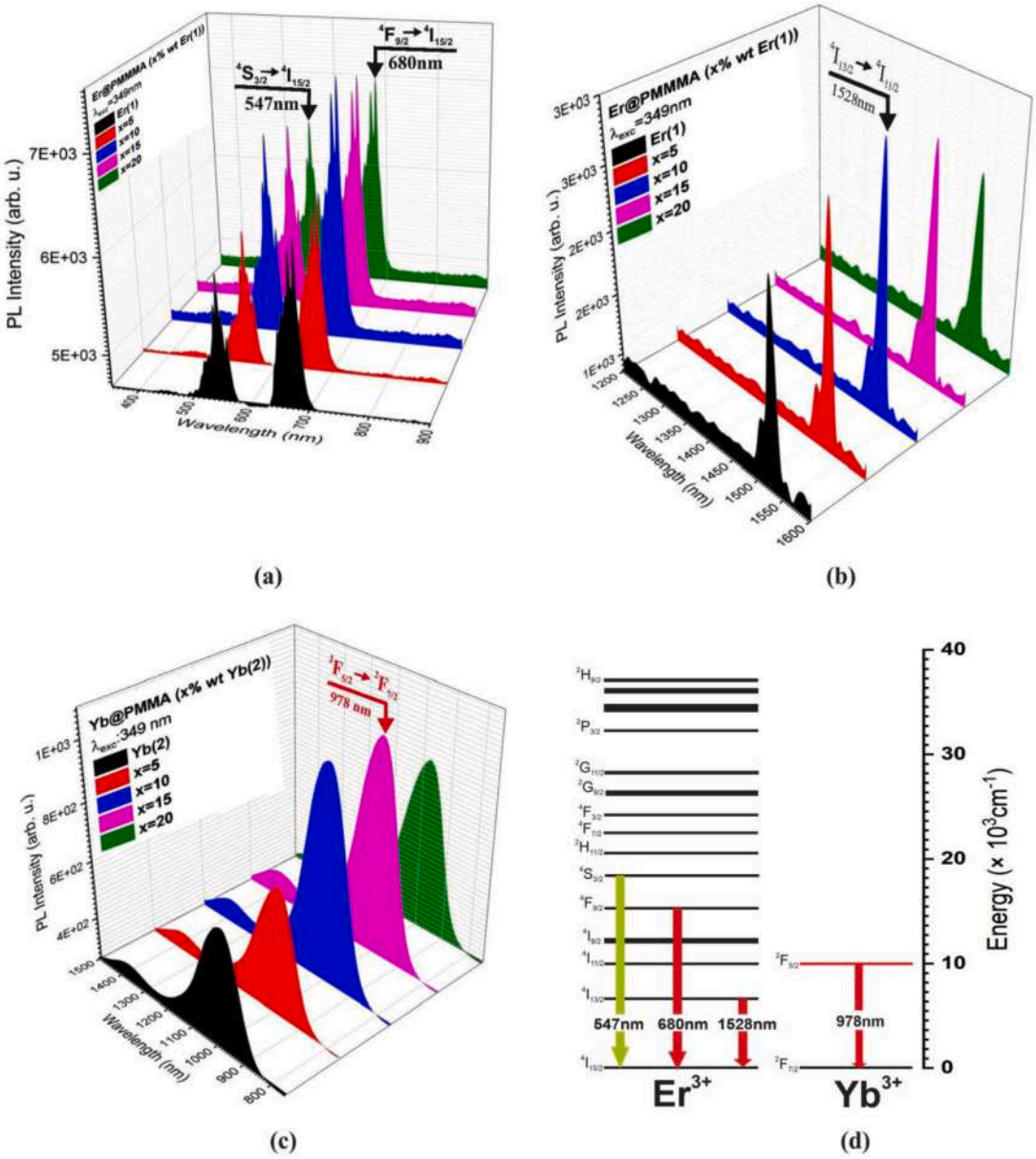

Fig. 6. The solid-state 3D PL intensity plots for Er@PMMA (a) Vis region (b) NIR region, (c) Yb@PMMA (NIR region) with varying Er(**1**) and Yb(**2**) concentrations (x = 5 to 20wt.%) at an excitation wavelength of 349 nm and (d) Possible mechanism of luminescence transition of Er^{3+} and Yb^{3+}.

at 10%. However, further increases in Ln^{3+} concentration result in a noticeable reduction in Ln^{3+} emission. As the Ln^{3+} content increases, the distance between Ln^{3+} ions decrease, leading to the phenomenon of concentration quenching.

The results illustrate that the optimal doping concentration for Er^{3+} ions is 0.15, while for Yb^{3+} ions it is 0.10. The analysis reveals that the luminescence intensity of Er^{3+}increases initially and reaches its maximum at 15% doping concentration, whereas the luminescence intensity of Yb^{3+} reaches its peak at 10%. However, the further increase in Ln^{3+} concentration leads to significant quenching of Ln^{3+} emissions. The phenomenon of concentration quenching occurs due to the decrease in the distance between Ln^{3+} ions as their concentration increases.

The possible luminescence transitions of Er^{3+} and Yb^{3+} are depicted in Fig. 6d. The processes behind the visible emissions of Er^{3+} ions when excited by 349 nm light are well-understood and involve two energy mechanisms: (i) excited state absorption and (ii) energy transfer. When the ground state $^4I_{15/2}$ of the Er^{3+} ion absorbs a photon with a wavelength of 349 nm, it transitions to the $^2G_{11/2}$ level through a process of ground state excitation. The $^4S_{3/2}$ state is populated by a multiphonon relaxation process, where some ions return to the ground state by radiative leap and emit green light, while the rest transition to the $^4F_{9/2}$ energy level via non-radiative leap and emit red light through multiphonon relaxation and subsequent radiative leap. According to our assumed NIR emission scenario, ions in the $^4I_{11/2}$ level decay radiatively or non-radiatively to the next lower level, $^4I_{13/2}$, and can relax radiatively to the $^4I_{15/2}$ level with 1.528 μm emission generated by the radiative relaxation process [38–40].

4. Conclusion

This study not only successfully synthesized and characterized $Er^{3+}$and Yb^{3+} complexes but also seamlessly integrated them into PMMA-based hybrid films through electrospinning, leading to significant enhancements in photoluminescence properties. This integration allowed for the Er@PMMA and Yb@PMMA composite fibers to exhibit intense photoluminescence upon ultraviolet excitation. Specifically,

Er^{3+} complexes displayed bright pink photoluminescence with prominent green and red emission peaks at 547 nm and 680 nm, respectively, while Yb^{3+} complexes showed substantial photoluminescence in the near-infrared (NIR) region, notably at 980 nm. The optimal doping concentrations were determined to be 15% for Er^{3+} and 10% for Yb^{3+}, striking a careful balance between enhancing luminescence intensity and preventing quenching effects due to excessive doping. The luminescence observed in Er^{3+} ions was effectively explained through mechanisms involving excited state absorption and energy transfer processes.

This research contributes critical insights into the luminescence mechanisms of these complexes, marking a significant step forward in the field of photoluminescent materials technology. It provides a comprehensive understanding of the materials' structural, thermal, and luminescent characteristics, highlighting the synergistic effects of embedding these complexes into a PMMA matrix. Consequently, this study represents a significant contribution to the field of luminescent materials, offering a promising approach for the development of high-performance, stable, and efficient photoluminescent materials. The insights gained not only advance our understanding of lanthanide-doped materials but also pave the way for their practical application across a range of technologies, emphasizing the critical role of interdisciplinary collaboration in the advancement of materials science. Future research should aim to optimize doping concentrations and explore alternative polymer matrices to further enhance the performance and broaden the application scope of these luminescent composites.

CRediT authorship contribution statement

Ugur Erkarslan: Visualization, Methodology. **Gorkem Oylumluoglu:** Visualization, Software. **Ozay Eroglu:** Visualization, Software, Conceptualization. **Mustafa Burak Coban:** Writing – review & editing, Writing – original draft. **Hulya Kara Subasat:** Writing – review & editing.

Declaration of competing interest

The authors declare that they have no known competing financial interests or personal relationships that could have appeared to influence the work reported in this paper.

Data availability

Data will be made available on request.

Acknowledgement

The authors thank to thank the Research Funds of Balikesir University (Grant No. BAP-2019/079) and Balikesir University for their generous financial support. We would like to thank Dokuz Eylul University for the use of the Agilent Xcalibur Eos diffractometer (purchased under University Research Grant No. 2010.KB.FEN.13) and Balikesir University, Science and Technology Application and Research Center (BUBTAM) for the use of the Photoluminescence Spectrometer.

Supplementary materials

Supplementary material associated with this article can be found, in the online version, at doi:10.1016/j.molstruc.2024.138633.

References

[1] B. Ay, E. Yildiz, İ. Kani, Semiconducting lanthanide polymers of pyridine-2,6-dicarboxylate: hydrothermal synthesis, structural characterization, electrical conductivity and luminescence properties, Polyhedron. 142 (2018) 1–8.
[2] T. Chuasaard, S. Thammakan, N. Semakul, T. Konno, A. Rujiwatra, Structure and photoluminescence of two-dimensional lanthanide coordination polymers of mixed phthalate and azobenzene dicarboxylate, J. Mol. Struct. 1251 (2022) 131940.
[3] Y. Acar, M.B. Coban, E. Gungor, H. Kara, Two New NIR Luminescencent Er(III) Coordination Polymers with Potential Application Optical Amplification Devices, J. Clust. Sci. 31 (2020) 117–124.
[4] F. Kuru, M.B. Coban, U. Erkarslan, A. Donmez, G. Oylumluoglu, M. Aygun, H. Kara Subasat, Improved photoluminescence properties of one-dimensional (1D) composite fibers of Ho@PVP and Yb@PVP prepared by electrospinning, Polyhedron. 242 (2023) 116492.
[5] C. Zhang, S. Wei, L. Sun, F. Xu, P. Huang, H. Peng, Synthesis, structure and photocatalysis properties of two 3D Isostructural Ln (III)-MOFs based 2,6-Pyridinedicarboxylic acid, J. Mater. Sci. Technol. 34 (2018) 1526–1531.
[6] J. Feng, H. Zhang, Hybrid materials based on lanthanide organic complexes: a review, Chem. Soc. Rev. 42 (2013) 387–410.
[7] H. Kara, G. Oylumluoglu, M.B. Coban, Photoluminescence Properties of a New Sm (III) Complex/PMMA Electrospun Composite Fibers, J. Clust. Sci. 31 (2020) 701–708.
[8] M.B. Coban, M.E. Diken, S. Dogan, H.Kara Subasat, Structural, Thermal, Optical and Antibacterial Properties of Co-doped (Dy3+/Eu3+): PEG + PVA Novel Transparent Hybrid Films, J. Inorg. Organomet. Polym. Mater. 33 (2023) 2924–2942.
[9] K. Yin, L. Zhang, C. Lai, L. Zhong, S. Smith, H. Fong, Z. Zhu, Photoluminescence anisotropy of uni-axially aligned electrospun conjugated polymer nanofibers of MEH-PPV and P3HT, J. Mater. Chem. 21 (2011) 444–448.
[10] K. Naveen Kumar, K. Sivaiah, S. Buddhudu, Structural, thermal and optical properties of Tb3+, Eu3+ and co-doped (Tb3++Eu3+): PEO+PVP polymer films, J. Lumin. 147 (2014) 316–323.
[11] X. Liu, P.X. Ma, Phase separation, pore structure, and properties of nanofibrous gelatin scaffolds, Biomaterials 30 (2009) 4094–4103.
[12] S. Jiang, Y. Chen, G. Duan, C. Mei, A. Greiner, S. Agarwal, Electrospun nanofiber reinforced composites: a review, Polym. Chem. 9 (2018) 2685–2720.
[13] M. Li, Z. Zhang, T. Cao, Y. Sun, P. Liang, C. Shao, Y. Liu, Electrospinning preparation and photoluminescence properties of poly (methyl methacrylate)/Eu3 + ions composite nanofibers and nanoribbons, Mater. Res. Bull. 47 (2012) 321–327.
[14] Mercury, Version 3.9, Cambridge Crystallographic Data Centre, 2016. Cambridge, UK, (2016).
[15] O.V. Dolomanov, L.J. Bourhis, R.J. Gildea, J.A.K. Howard, H. Puschmann, OLEX2: a complete structure solution, refinement and analysis program, J. Appl. Crystallogr. 42 (2009) 339–341.
[16] A.L. Spek, Structure validation in chemical crystallography, Acta Crystallogr. Sect. D Biol. Crystallogr. 65 (2009) 148–155.
[17] M.B. Coban, E. Gungor, Y. Acar, F. Kuru Alpaslan, H.Kara Subasat, Eu@PMMA and Sm@PMMA nanofibers prepared by electrospinning: structure, morphology, luminescence and magnetic properties, CrystEngComm. 22 (2020) 6116–6127.
[18] A. DÖNMEZ, U. ERKARSLAN, Ş. KARADENİZ, Evropiyum içeren lüminesans özelliği gösteren metal-organik malzemelerin üretimi ve yapılarının araştırılması, Balıkesir Üniversitesi Fen Bilim. Enstitüsü Derg. 19 (2017) 64–69.
[19] A. Hernandez, J. Jenkins, H. Maslen, M. Zeller, G. Horner, C. Dempsey, J. Urteaga, C. Dunlap, R.A. Zehnder, Stress compensation in an extended series of lanthanide 2-sulfonatoterephthalates [Ln(TPSO3)(H2O)2]n (Ln = Ce − Lu, except Pm), Inorganica Chim. Acta 471 (2018) 104–112.
[20] U. Erkarslan, A. Donmez, H. Kara, M. Aygun, M.B. Coban, Synthesis, Structure and Photoluminescence Performance of a New Er3+-Cluster-Based 2D Coordination Polymer, J. Clust. Sci. 29 (2018) 1177–1183.
[21] M.R. Mas Haris, S. Kathiresan, S. Mohan, FT-IR and FT-Raman Spectra and Normal Coordinate Analysis of Poly methyl methacrylate, Der Pharma Chem 2 (2010) 316–323.
[22] M.O. Bensaid, L. Ghalouci, S. Hiadsi, F. Lakhdari, N. Benharrats, G. Vergoten, Molecular mechanics investigation of some acrylic polymers using SPASIBA force field, Vib. Spectrosc. 74 (2014) 20–32.
[23] H. Gu, Y. Hou, F. Xu, S. Wang, Electrospinning preparation, thermal, and luminescence properties of Eu2(BTP)3(Phen)2 complex doped in PMMA, Colloid Polym. Sci. 293 (2015) 2201–2208.
[24] P. Chen, M. Chai, Z. Mai, M. Liao, X. Xie, Z. Lu, W. Zhang, H. Zhao, X. Dong, X. Fu, F. Ko, X. Shi, W. Zheng, W. Zhou, Electrospinning polyacrylonitrile (PAN) based nanofiberous membranes synergic with plant antibacterial agent and silver nanoparticles (AgNPs) for potential wound dressing, Mater. Today Commun. 31 (2022) 103336.
[25] M.B. Coban, E. Gungor, Y. Acar, F.K. Alpaslan, H.K. Subasat, Multifunctional Dy@PVP and Ho@PVP one-dimensional nanofibers: electrospinning synthesis, luminescent and magnetic properties, J. Mol. Struct. 1272 (2023) 134117.
[26] P. Kumar, S. Singh, I. Gupta, K. Nehra, V. Kumar, D. Singh, Structural and luminescent behaviour of Dy(III) activated Gd3Al5O12 nanophosphors for white-LEDs applications, Mater. Chem. Phys. 295 (2023) 127035.
[27] P. Kumar, S. Singh, I. Gupta, K. Nehra, V. Kumar, D. Singh, Structural refinement and optical characteristics of single-phase Gd3Al5O12:Er3+ nanophosphors for luminescent applications, J. Lumin. 252 (2022) 119338.
[28] Q.F. Li, D. Yue, W. Lu, X. Zhang, C. Li, Z. Wang, Hybrid luminescence materials assembled by [Ln(DPA) 3]3- and mesoporous host through ion-pairing interactions with high quantum efficiencies and long lifetimes, Sci. Rep. 5 (2015) 1–9.
[29] C.H. Gao, L. Zhang, G.F. Hou, D.S. Ma, W.H. Jiang, Y.H. Yu, Syntheses, structures and properties of chiral Ln(III) coordination polymers based on (R)-4-(4-(1-carboxyethoxy)phenoxy)-3-fluorobenzoic acid, Inorg. Chem. Commun. 78 (2017) 70–73.

[30] E. Gungor, M.B. Coban, H. Kara, Y. Acar, Photoluminescence and Magnetism Study of Blue Light Emitting the Oxygen-Bridged Open-Cubane Cobalt(II) Cluster, J. Clust. Sci. 29 (2018) 967–974.
[31] M.B. Coban, E. Gungor, H. Kara, U. Baisch, Y. Acar, New mixed valence defect dicubane cobalt(II)/cobalt(III) complex: synthesis, crystal structure, photoluminescence and magnetic properties, J. Mol. Struct. 1154 (2018) 579–586.
[32] Y. Li, X. Li, D. Zhang, M. Wang, Upconversion luminescence enhancement and photochromic regulation of mononuclear β-NaYF4: Yb, Er, Opt. Mater. (Amst). 149 (2024) 115103.
[33] S. Wu, Y. Yang, S. Wu, Y. Dong, H. Cui, D. Li, W. Qin, Enhanced downconversion luminescence of NaLuF4:Yb3+,Er3+ micrometer hexagonal prismatic crystals under 980 nm excitation, J. Fluor. Chem. 274 (2024) 110252.
[34] H. Liu, J. Zhao, L. Huang, S. Zhao, S. Xu, Luminescence properties of Er3+ doped high density germanate glass scintillators for X-ray computed tomography (CT), Ceram. Int. 50 (2023) 8535–8538.
[35] M. Kaczkan, M. Malinowski, A. Suchocki, Cooperative luminescence of Yb 3 + ions in multisite YAM crystal, 265 (2024).
[36] M. Wujczyk, A. Watras, K. Szyszka, R.J. Wiglusz, Influence of vanadium concentration on up-conversion luminescence in Er3+–Yb3+ and Tm3+–Yb3+ ions pair co-doped YVxP1−xO4 solid state solution, J. Alloys Compd. 884 (2021) 161022.
[37] J. Wu, H.Y. Li, Q.L. Xu, Y.C. Zhu, Y.M. Tao, H.R. Li, Y.X. Zheng, J.L. Zuo, X.Z. You, Synthesis and photoluminescent properties of series ternary lanthanide (Eu(III), Sm (III), Nd(III), Er(III), Yb(III)) complexes containing 4,4,4-trifluoro-1-(2-naphthyl)-1,3-butanedionate and carbazole-functionalized ligand, Inorganica Chim. Acta 363 (2010) 2394–2400.
[38] R.K. Tamrakar, D.P. Bisen, N. Brahme, I.P. Sahu, K. Upadhyay, Structural and luminescence behavior of Gd2O3:er3+ phosphor synthesized by solid state reaction method, Optik. (Stuttg) 126 (2015) 2654–2658.
[39] J. Ling, J. Wang, J. Zhang, H. Du, Q. Zong, J. Chen, The temperature sensing characteristics of Ba0.60Sr0.40TiO3: x% Er3+ powders based on upconversion luminescence, Opt. Mater. (Amst). 128 (2022) 112421.
[40] T. Wei, F. Chen, Y. Tian, S. Xu, Efficient 2.7μm emission and energy transfer mechanism in Er3+ doped Y2O3 and Nb2O5 modified germanate glasses, J. Quant. Spectrosc. Radiat. Transf. 133 (2014) 663–669.